Nanoscale chemical and mechanical heterogeneity of human dentin characterized by AFM-IR and bimodal AFM

Lijia Huang [a,b,1], Xiaoyue Zhang [c,d,1], Jian Shao [c], Ziyu Zhou [a], Yanan Chen [a], Xiaoli Hu [a,b,*]

[a] Department of Operative Dentistry and Endodontics, Guanghua School of Stomatology, SunYat-sen University, Guangzhou 510000, China
[b] Guangdong Provincial Key Laboratory of Stomatology, Sun Yat-sen University, Guangzhou 510000, China
[c] State Key Laboratory of Optoelectronic Materials and Technologies, School of Physics, Sun Yat-sen University, Guangzhou 510275, China
[d] Micro and Nano Physics and Mechanics Research Laboratory, School of Physics, Sun Yat-sen University, Guangzhou 510275, China

HIGHLIGHTS

- AFM-IR technique was used to detect the chemical heterogeneity of human dentin for the first time.
- The heterogeneity of mechanical properties of human dentin was explored by AFM AM-FM technique.
- A band at 1336 cm^{-1} assigned to S=O stretching vibrations was found only in peritubular dentin.
- Peritubular dentin had a higher Young's modulus (32.25 ± 4.67 GPa) than intertubular dentin.
- AFM-IR and AFM AM-FM are useful for understanding the mineral deposition mechanisms of dentin.

GRAPHICAL ABSTRACT
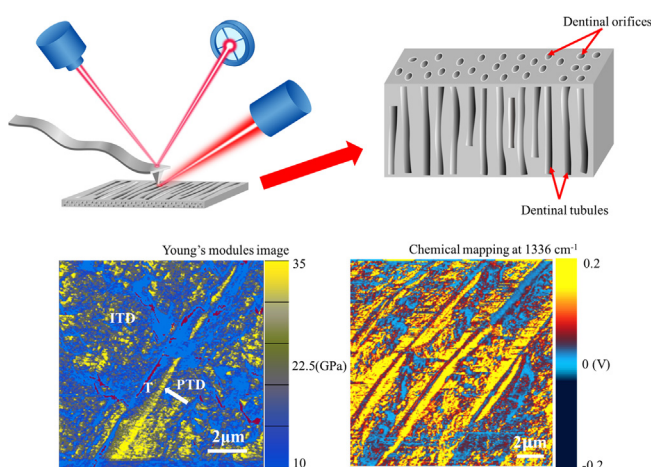
ARTICLE INFO

ABSTRACT

Human dentin, as an important calcified tissue in the body, plays significant roles in withstanding masticatory forces and has a complex hierarchical organization. Understanding the composition and ultrastructure of dentin is critical for elucidating mechanisms of biomineralization under healthy and pathological states. Here, atomic force microscope infrared spectroscopy (AFM-IR) and AFM-based amplitude modulation-frequency modulation (AM-FM) techniques were utilized to detect the heterogeneity in chemical composition and mechanical properties between peritubular and intertubular dentin at the nanoscale. AFM-IR spectra collected from peritubular and intertubular dentin contained similar vibrational bands in the amide regions (I, II and III), suggesting that collagen may exist in both structures. A distinctive band at 1336 cm^{-1} indicative of S=O stretching vibrations was detected only in peritubular dentin. AFM-IR imaging showed an uneven distribution of chemical components at different locations, confirming the heterogeneity of dentin. The Young's modulus of peritubular dentin was higher, and was associated to a higher mineral content. This study demonstrated distinctive chemical and mechanical properties of peritubular dentin, implying the different development and mineralization processes

between peritubular and intertubular dentin. AFM-IR is useful to provide compositional information on the heterogeneity of human dentin, helping to understand the mineral deposition mechanisms of dentin.

Introduction

Dentin, which comprises most of tooth structure, is a mineralized connective tissue with distinctive mechanical properties necessary for supporting enamel, protecting dental pulp and withstanding masticatory forces without fracturing [1,2]. Like other vertebrate mineralized tissues such as dental enamel and bone, the specialized functions of dentin are determined by its hierarchical organization and composition [3]. Dentin is a heterogeneous composite material traversed by dentinal tubules of micrometer diameter (1–2 μm) and surrounded by mineralized peritubular dentin, which is embedded within a partially mineralized intertubular dentin [4,5]. The dentin tubules extend radially outwards from the pulp toward the dentin-enamel junction (DEJ) and cementum-dentin junction (CDJ) [2,5]. The heterogeneity of this human hard tissue makes it difficult to be repaired and reconstructed readily [6]. Clinically, dentin damaged by disease has to be replaced by restorations. Understanding the mechanical and biochemical properties of dentin is the cornerstone to predicting its behavior and its interfacial interactions with restorations [5,7]. Such knowledge will help to reveal the process of mineral deposition, which is important for the development of treatments for mineralization-related diseases (dentinogenesis imperfecta, dental erosion and carious lesions) and also for the innovation and development of scaffolds for its repair.

Due to the small dimensions of human peritubular dentin (about 1 μm in width) and its being contiguous with intertubular dentin [8], the chemical composition and structure of peritubular dentin is still not well understood. FTIR spectroscopy was an excellent tool for analyzing the functional group of organic and inorganic molecules, as well as crystallinity of the mineralized tissue [9–15]. The organic and mineral composition of peritubular dentin of horses has been identified using fourier transform infrared spectroscopy (FTIR) [16]. Due to the limited spatial resolution (3–30 μm) of FTIR, conventional FTIR spectroscopy of human teeth only represents the average spectrum within a beam area consisting of both peritubular and intertubular dentin and fails to distinguish peritubular dentin from intertubular dentin [16–18]. AFM-based infrared spectroscopy (AFM-IR) is a new technique which combines the spatial resolution of atomic force microscopy (AFM) with the chemical analysis of infrared spectroscopy (IR) using the AFM probe to detect the changes of photothermal resonance induced by pulsed infrared emissions. The AFM-IR technique can achieve chemical component mapping with high spatial resolution of 20–30 nm, which is also in high consistency with FTIR [17–19]. Taking the advantage of the fine spatial resolution and the ability to collect topographical and chemical information simultaneously, AFM-IR technique is the ideal tool for identifying the structural heterogeneity of nanocomposite materials and tissue samples including dentin, bone, skin and hair [20–30].

The difference in chemical distribution between peritubular and intertubular dentin may induce differences in mechanical properties. Clarifying the mechanical differences between peritubular and intertubular dentin is the corroboration for the chemical difference, as well as an important reference for dental operative procedures. Previous articles have reported the Young's modulus difference between peritubular and intertubular dentin via techniques such as nanoindentation and AFM-indentation [31,32]. However, the spatial resolution of the above approaches is also limited. Instead, AM-FM mode is a recently developed bimodal AFM technique that provides fast and quantitative maps of Young's modulus and viscosity coefficients of the sample surface with comparable spatial resolution with AFM-IR mapping [33,34]. In AM-FM mode, the cantilever was excited at two frequencies simultaneously. The first-order resonance was used for tapping mode imaging, which was operated in amplitude modulation (AM). As the tip taps the surface, the second resonance frequency will shift depending on how the tip interacts with the sample. This frequency shift is traced with frequency modulation (FM) and converted into values of the sample's Young's modulus. AM-FM mode has been applied to determine elastic modulus of a large variety of materials such as bone microconstituents, cells and polymers [34], which will benefit the study of the differences in mechanical properties between peritubular and intertubular dentin.

This is the first study to identify the nanoscale chemical heterogeneity of human dentin by AFM-IR. Using the non-invasive, non-destructive AFM-IR technique, we obtained the IR absorption spectra at nanoscale, providing information of the chemical composition of human peritubular and intertubular dentin. Additionally, AFM-IR is able to provide the nanoscale chemical imaging to characterize the organic and mineral distribution in human dentin. In this study, we tested whether the chemical and mechanical properties of human peritubular dentin are different from intertubular dentin, and whether AFM-IR is a useful tool to identify the nanoscale chemical heterogeneity of human dentin.

Material and methods

Specimen preparation

Human third molars were obtained from patients between ages of 18 and 30 at the Hospital of Stomatology, Sun Yat-sen University, as approved by the Research Ethics Committee (ERC-[2017]-18). The teeth were without any caries, cracks or other defects. The molars were stored in 0.9% phosphate buffered saline (PBS) solution (pH = 7.4) containing 0.002% sodium azide at 4 °C. The roots were removed with a slow-speed water cooled diamond saw (Buehler Ltd., Lake Bluff, IL, USA). The remaining tooth samples were sectioned longitudinally into beams of about 3.0 mm × 6.0 mm × 3.0 mm (Fig. 1). The dentin beams were mechanically fractured to avoid creation of a smear layer on cut surfaces. To be specific, two notches were made in the opposite sides of a dentin beam and it was then plunged into liquid nitrogen for 10 min and fractured along the line joining the notches.

SEM observation

The dentin specimens described above were dehydrated in ascending grades of acetone (from 25% to 100%). Excess acetone was permitted to evaporate under a protective hood and the specimens subsequently coated with platinum (Pt) for 3 min. Observations were carried out with an FE-SEM (Ultra Zeiss Oberkochen, Germany) at 1–5 kV under an in-lens detector.

Fourier transform infrared (FTIR) spectroscopy

Three different spots on the surface of a specimen were randomly chosen and ATR-FTIR spectra were collected using the
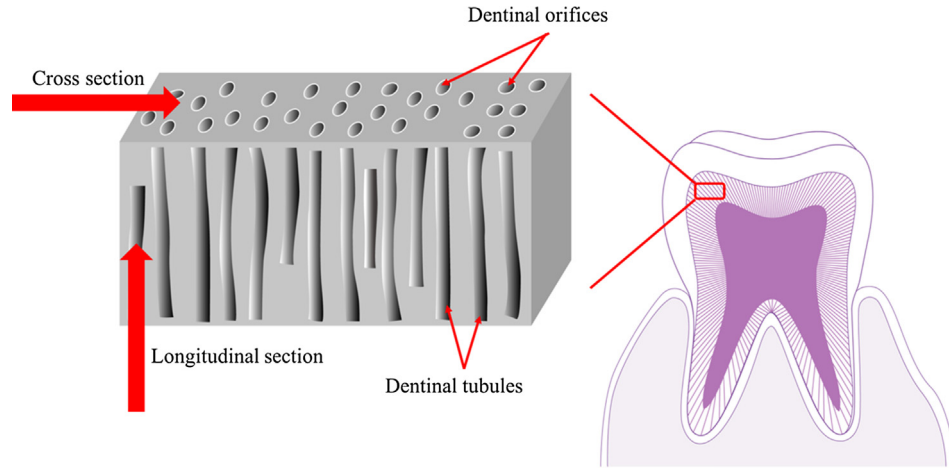
Fig. 1. Schematic diagram showing the preparation of dentin specimen.

Thermo Nicolet 5700 spectrometer (Nicolet, Madison, WI). To be specific, the specimen was place on the face of the germanium crystal of the smart OMNI sampler accessory (Nicolet, Madison, WI) and the pointed tip of the standard pressure tower was adjusted to the center of the mark. Spectra were collected in the range from 750 to 4000 cm^{-1} at 4 cm^{-1} resolution by using 100 scans. The peaks ranging from 900 to 1800 cm^{-1} of the dentin specimen were recorded according to Bachmann et al [35,36].

X-ray diffraction (XRD)

The X-ray diffraction (XRD) analysis was performed to explore the crystallinity phases of dentin. The XRD profiles were recorded with a diffractometer (PANalytical-Empyrean instrument) using a step size of 0.02° mrad/s and a scan range 2θ of 20–40°. The voltage and current were 40 kV and 40 mA respectively.

Atomic force microscope infrared spectroscopy (AFM-IR)

The IR absorption spectra were obtained using the Nano-IR2s instrument (Anasys Instruments, Santa Barbara, CA) (https://www.bruker.com/products/surface-and-https://www.bruker.com/products/surface-and- dimensional-analysis/nanoscale-infrared-spectrometers.html). The instrument consists of a tunable infrared laser focusing onto a sample in the proximity of the AFM probe tip. At each wavenumber of the laser, the oscillation amplitude of AFM cantilever is recorded to achieve IR absorption of the specimen. It is reported that the AFM cantilever oscillation amplitude is linearly dependent on the IR absorption. For each characterization, the focusing spot of the laser was tuned to optimize the oscillation amplitude of AFM cantilever. The specimen was fixed upon a metal plate with adhesive tape in between. The AFM scans in the AFM-IR were carried out in contact mode with a PR-EX-nIR2 gold-coated cantilever (resonance frequency: 13 kHz, spring constant: 0.23 N/m). To enhance oscillation amplitude of AFM cantilever, the pulse frequency of the laser was synchronized and locked to the resonant frequency of the tip in contact with the specimen.

The single IR spectrum data were collected at selected sites with a wavenumber spacing of 2 cm^{-1}. The incident laser power was set to 80% in the range from 900 cm^{-1} to 1800 cm^{-1}. The IR spectra were normalized to a fixed laser power at each wavenumber via calibrating with the laser power detected by an IR sensitive photodetector. The spectra were smoothed in Analysis Studio, a software from Anasys Instruments. The baseline for each spectrum was determined through local minimum fitting. Then the baselines were subtracted to remove interference from IR absorbance in substrate and thick sample. The parameters including mineral/protein ratio, crystallinity and acid phosphate content were assessed on basis of the corrected spectra [37].

For the IR chemical mapping, the laser power was adjusted to 82.4% for the mapping at 1033 cm^{-1}, 1336 cm^{-1}, 1692 cm^{-1}. For all IR mapping, the scan rate was 0.2 Hz. Meanwhile, the topography images were recorded during mapping to keep the track of the specimen drifting. The 1692 cm^{-1}/1033 cm^{-1} intensity ratio map was generated from the 1692 cm^{-1} and 1033 cm^{-1} maps after the image shift correction.

Mechanical properties mapping

Mechanical properties of the dentin specimen were obtained in-situ with AM-FM mode via an Asylum Research MFP-3D Infinity AFM system. In AM-FM mode, the cantilever is excited near the first and second resonant frequencies simultaneously. The first-order resonance is operated in AM mode for morphology imaging. To be specific, the cantilever is excited near the first resonant frequency f_1. The deflection signal of the cantilever is analyzed by a lock-in amplifier to determine the amplitude A_1 and phase ϕ_1 response of the first eigenmode. During the scanning, the feedback loop adjusts A_1 to maintain constant that equal to amplitude setpoint $A_{1,set}$, so that the displacement of scanner in z-direction can be used for morphology tracking. Meanwhile, the cantilever is also excited at the second resonant frequency f_2. Here, a frequency feedback loop adjusts the frequency by a small amount Δf_2 to maintain the second eigenmode on resonance as the tip interacts with the sample.

The AM-FM signals were recorded by the lock-in and feedback system and can be used to extract the indentation depth [34,38]

$$\delta = \frac{3}{4}\left(\frac{k_1}{Q_1}A_{1,free}\cos\phi_1\right)\left(\frac{2k_2\Delta f_2}{f_2}\right)^{-1}$$

and effective storage modulus

$$E_{eff} = \frac{\pi}{R}\sqrt{\frac{1}{6}}\left(\frac{k_1}{Q_1}\frac{A_{1,free}}{A_{1,set}}\cos\phi_1\right)^{-\frac{1}{2}}\left(\frac{2k_2\Delta f_2}{f_2}\right)^{-\frac{2}{3}}$$

where Q_1, $A_{1,free}$ are the quality factor and A_1 of the cantilever in air under first resonant frequency, which can be obtained by the tuning procedure. k_1 and k_2 are the modal stiffness of the cantilever. k_1 can be obtained by force constant calibration. k_1 can be calculated by $k_2 = \left(\frac{f_2}{f_1}\right)^2 k_1$.

In this work, AC160TS-R3 probe (Olympus Ltd Tokyo, Japan) was adopted for AM-FM imaging. The force constant (modal stiffness of the first resonant frequency) of the probe was calibrated using the thermal noise method to be $k_1 = 26.125$ N/m. And its first and second resonance frequency was 270 kHz, and 1504 kHz respectively. Thus $k_2 = 810.758$ N/m was obtained. The tip has a typical tip radius of 7 nm. The fractured dentin with exposed longitudinal section was scanned directly in AM-FM mode without preliminary treatment. The scan speed was set at 0.5 line/s, and $A_{1 free}$ was chosen to be 100 nm. Because the actual value of tip radius is difficult to know, AM-FM mode usually need a reference sample of known modulus to calibrate the tip radius. We used a clean glass slide as reference sample, which has a Young' modulus of 55 GPa [39]. And the tip radius was calibrated to be 8 nm. Schematic diagrams of methodology for AFM-IR and Bimodal AM-FM were shown in Fig. 2.

Results and discussion

Spectral characterizations of peritubular and intertubular dentin

To confirm the sample preparation procedure exposes the dentin surface correctly, we observed the fractured dentin surface with SEM. The typical image with dentinal tubules perpendicular to the surface is shown in Fig. 3. The dentin tubules, seen in transverse cross section, are surrounded by peritubular dentin and connected by intertubular dentin. The peritubular dentin appears as ring-like structures and is distinguished from intertubular dentin by its appearance being brighter, more dense and smoother; while the intertubular dentin seems more disorganized and rugged and (as seen in Fig. 3B), seemed tightly packed with fibers. The average width of the peritubular dentin is about 1.31 ± 0.18 μm, which were in accordance with previous reports [4,7,40].

To clarify the chemical distribution difference between peritubular and intertubular dentin, IR absorption spectra of the peritubular dentin and the intertubular dentin were obtained using the nano-IR in the range from 900 to 1800 cm^{-1} (Fig. 4). The spectrum, without background modification, is available in Fig. S1 as an attachment. The absorption bands associated with the organic contents at 1532 and 1596 cm^{-1} are assigned to amide II; the peak at around 1692 cm^{-1} assigned to amide I, at around 1206, 1254, 1280 and 1360 (1380) cm^{-1} assigned to amide III, at around 1336 cm^{-1} assigned to S=O stretching vibrations (sulfonamide) [1,4,16,41–53]. The absorption peaks associated with mineral contents at around 932, 966, 1033, 1088, 1148, 1442 and 1490 cm^{-1}, are assigned to $PO_4^{3-} v_1$, $PO_4^{3-} v_1$, $PO_4^{3-} v_3$, $PO_4^{3-} v_3$, HPO_4^{2-}, $CO_3^{2-} v_3$ and $CO_3^{2-} v_3$, respectively [4,16,41,42,46].

The detailed information about the locations and assignments of AFM-IR spectra from intertubular dentin and peritubular dentin is listed in Table 1. Several absorption bands were observed both in peritubular and intertubular dentin spectra (Table 1). As the amide I and III bands were typical of collagen, our study supported that peritubular dentin contains collagen, which was also observed by other researchers [4,16]. Besides the peaks assigned amide I, amide II and amide III, a unique band at 1336 cm^{-1} assigned to the S=O stretching modes of sulfonamide [45], was detected in peritubular dentin. As chondroitin sulfate has been identified by immnunohistochemistry [54], it was speculated the 1336 cm^{-1} band in peritubular dentin may be originated from chondroitin sulfate. Chondroitin sulfate, a sulfated glycosaminoglycan on cell surfaces and within pericellular matrices in the form of proteoglycans, plays an important role in various physiological and pathological processes [55]. In addition, a unique band of 1490 cm^{-1} assigned to $CO_3^{2-} v_3$ was observed only in peritubular dentin, indicating that peritubular dentin may contain a greater variety of inorganic contents than intertubular dentin. When analyzing the FTIR spectrum
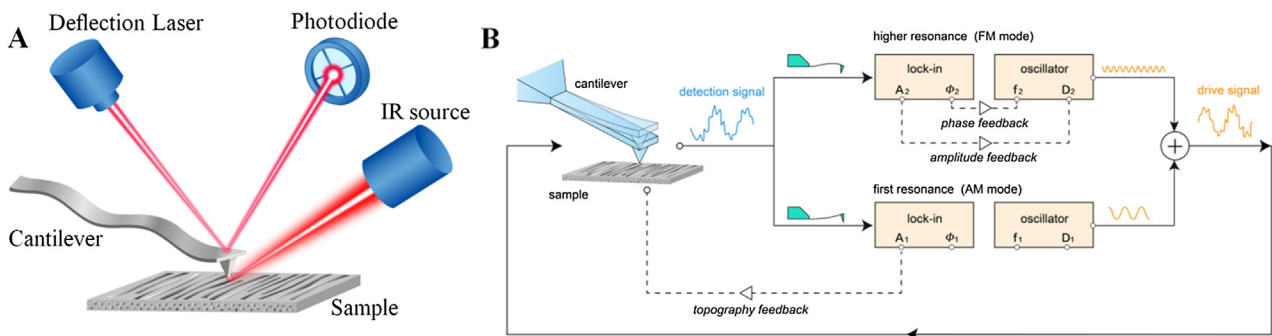

Fig. 2. Schematic diagrams of methodology for AFM-IR and Bimodal AFM. (A) Schematic diagram for AFM-IR. (B) System diagram for bimodal AM-FM imaging mode.
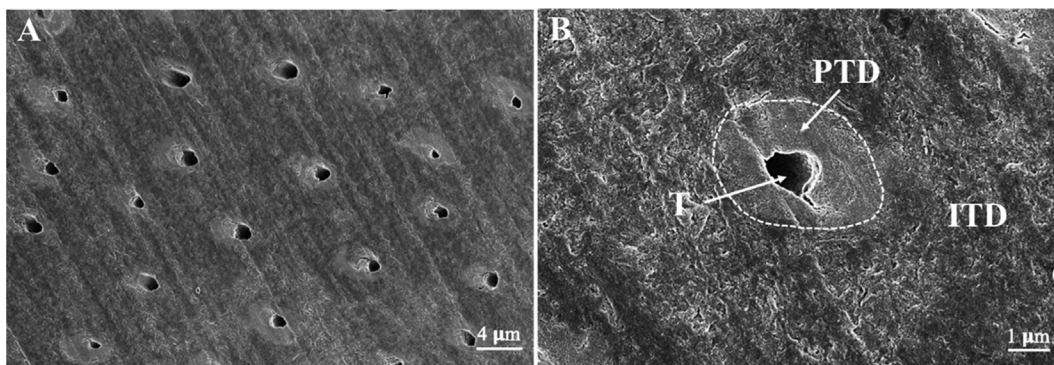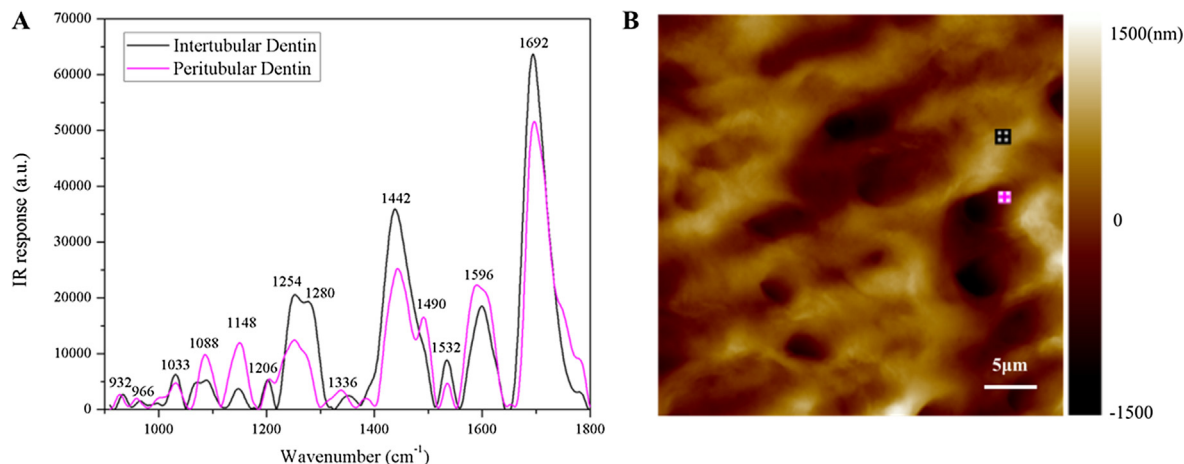

Fig. 3. Scanning electron microscope (SEM) images of dentin surfaces. (A) SEM image of dentin surface seen in transverse cross section. (B) The dentin tubule (T) is surrounded by peritubular dentin (PTD) and connected by intertubular dentin (ITD).

Fig. 4. AFM-IR spectra collected from peritubular dentin and intertubular dentin. (A) The IR spectra for the region of 900–1800 cm^{-1}. The color of the spectra corresponds to the spots indicated in B. (B) AFM image showing the height of sample.

Table 1
Wavenumbers (cm^{-1}) and peak assignments of nano-IR spectra from intertubular dentin and peritubular dentin.

PTD (cm^{-1})	ITD (cm^{-1})	Assignment
932	932	PO$_4^{3-}$-v_1 [4,42,46]
966	966	PO$_4^{3-}$-v_1 [4,41,42,46]
1033	1033	PO$_4^{3-}$-v_3 [16,41,46]
1088	1088	PO$_4^{3-}$-v_3 [4,16,46]
1148	1148	HPO$_4^{2-}$ [16,46]
1206	1206	Amide III [16,48,49,52]
1254	1254	Amide III [16,41,43,47–49,52]
1280	1280	Amide III [1,4,16,47–49,52]
1336		S=O stretching vibrations [45]
1380	1360	Amide III [44,48,49,52]
1442	1442	CO$_3^{2-}$-v_3 [41,42]
1490		CO$_3^{2-}$-v_3 [16,41,42]
1532	1532	Amide II [41–43,49,52,53]
1596	1596	Amide II [46,49,51,53]
1692	1692	Amide I [16,41–43,48–50,52,53]

of human dentin (Fig. S2), we found that all absorption peaks in FTIR spectrum were also found in the AFM-IR spectra. The shift between FTIR and AFM-IR spectra was slight. More details of absorption peaks were observed in AFM-IR spectra, indicating the higher resolution of local IR characterization. XRD profile of dentin could be accessed in Fig. S3 as an attachment file. As indicated by Fig. S3, the diffraction peak (0 0 2) at 2θ = 25.90°, (2 1 1) at 2θ = 31.77°, (1 1 2) at 2θ = 32.19° and (3 0 0) at 2θ = 32.90°are all characteristic peaks of hydroxyapatite (HA) crystals according to International Centre for Diffraction Data (ICDD). However, it is important to point out that XRD analysis can only provide the average inorganic information of dentin and cannot distinguish peritubular dentin from intertubular dentin [56–62].

As shown by IR spectrum, the intensity of 932, 966, 1088 and 1148 cm^{-1} band of peritubular dentin is higher than that of intertubular dentin. The mineral/protein (PO$_4^{3-}$-v_1v_3/amide I) ratio (932/1692 cm^{-1}, 966/1692 cm^{-1}, 1033/1692 cm^{-1} and 1088/1692 cm^{-1}) of peritubular dentin is found to be significantly higher than that of intertubular dentin (p < 0.01), indicating that peritubular dentin has more mineral content than intertubular dentin. Crystallinity and acid phosphate content are useful for understanding the mineralization process. Crystallinity, which is an index of crystal size/perfection, represents the degree of long range order of material and strongly affects its quality [63]. As measured by the 1033/1020 cm^{-1} ratio, the crystallinity of inter-

tubular dentin (1.20 ± 0.02) is significantly higher than that of peritubular dentin (1.06 ± 0.01) (p < 0.01), indicating that intertubular dentin contained more highly crystalline apatite. The acid phosphate content (1148/1088 cm^{-1}) is significantly greater for peritubular dentin (1.24 ± 0.01) than for intertubular dentin (0.87 ± 0.01) (p < 0.01).

Generally, increasing the degree of crystallinity indicates a relatively lower degree of imperfections, disorders and substitutions [63]. In our study, the crystallographic structure of peritubular dentin was found to be lower than that of intertubular dentin, meaning that although peritubular dentin is highly calcified, the calcified material may not be apatite mineral [54,63,64]. As reported before, the types of mineralization in majority of dentin was extracellular matrix (ECM) molecular-derived mineralization, including extrafibrillar and intrafibrillar mineralization [65,66]. For intertubular dentin, non-mineralized predentin formation preceded maturation of dentin [66]. Peritubular dentin did not result from such transformation of predentin into dentin. Proteoglycans, lipids and other ECM proteins were in the formation of a thin amorphous network, leading to a dense hypermineralized peritubular dentin [66]. Besides, when considering the mechanism of biological hydroxyapatite formation of dentin, the mineral nucleation and mineral propagation can be expected to differ between these two structures. Further study of these conjectures needs to be carried out.

AFM-IR imaging of peritubular and intertubular dentin

To reveal the distribution of each chemical component, IR chemical mapping was conducted on longitudinal section of dentin, in which the IR source was respectively tuned to 1033 cm^{-1} corresponding to PO$_4^{3-}$-v_3, 1336 cm^{-1} corresponding to S=O stretching vibrations (sulfonamide), and 1692 cm^{-1} corresponding to amide I (Fig. 5). The distribution of PO$_4^{3-}$-v_3 and S=O stretching vibrations (sulfonamide), as well as amide I are uneven between peritubular and intertubular and dentin. As shown in Fig. 5A and 5B, PO$_4^{3-}$-v_3 and S=O stretching vibrations (sulfonamide) typically exhibit relative high intensity (dark yellow signal) in peritubular dentin, whereas light red and blue PO$_4^{3-}$-v_3 and S=O stretching vibrations (sulfonamide) signals suggest a relative low intensity in intertubular dentin. In Fig. 5C, the intertubular dentin shows intense amide I signal, while peritubular dentin exhibits relative weak amide I intensity. The chemical mapping images allow for
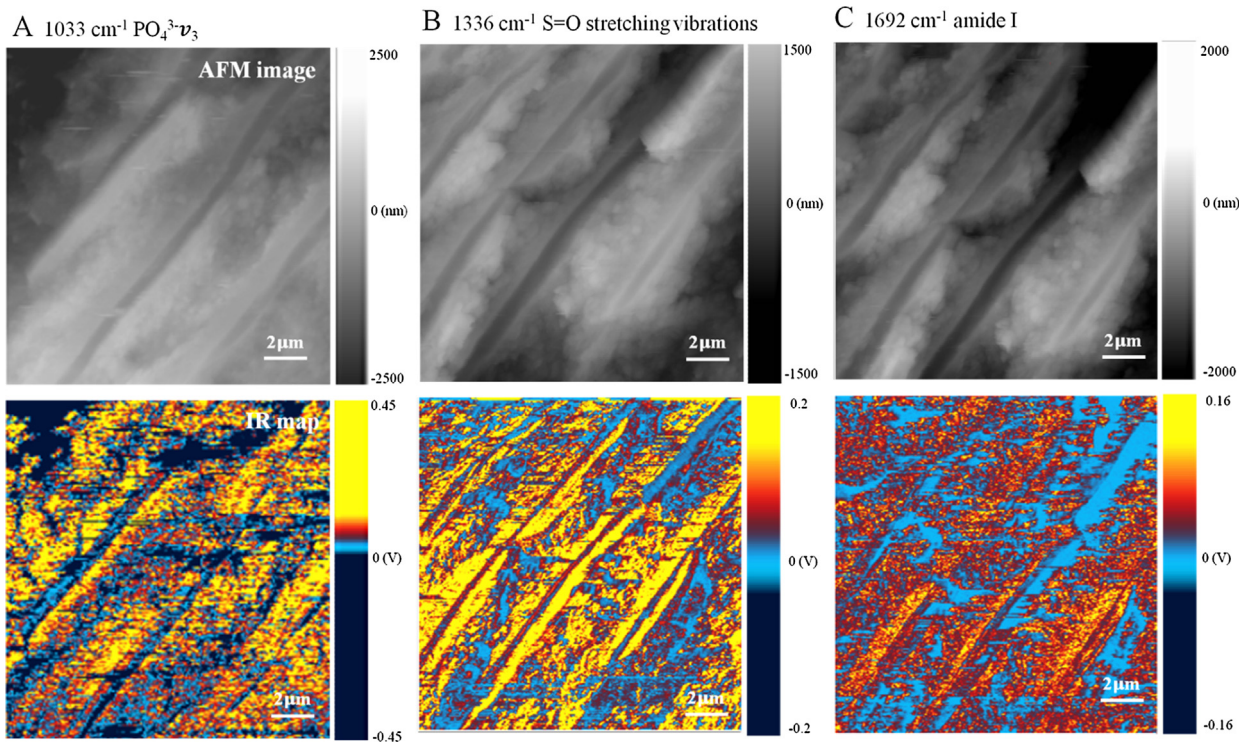
Fig. 5. IR map of human dentin for each frequency coupled with corresponding AFM image which was captured during the mapping measurement to keep track of the sample drift. Area are 15×15 μm^2. (A) PO_4^{3-}-v_3 at 1033 cm^{-1}. (B) S=O stretching vibrations at 1336 cm^{-1}. (C) Amide I at 1692 cm^{-1}.

the visualization of distribution of various aggregates in peritubular dentin and intertubular dentin.

The results of Fig. 5 were consistent with the result of Fig. 4A indicated by the IR spectrum. The finding of low intensity of amide I in human peritubular dentin compared to intertubular dentin in this study was consistent with the previous studies [4,8,16]. To be specific, the mineral content of peritubular dentin was much more abundant than that of intertubular dentin, while the organic matter of peritubular dentin was much less than that of intertubular dentin [4]. Hard tissues in vertebrate animals, such as dentin, bone and cementum are generated by mesenchymal cells that express a matrix of fibrillar collagen type I, which mineralizes through the introduction of apatite nanocrystals into the fibrils and into the extrafibrillar space [8]. As previous studies showed that peritubular dentin forms from an extracellular matrix rich in glutamic acid, it is considered an exception among mineralized tissues [67,68].

Fig. 6 shows the amide I/PO_4^{3-}-v_3 peak intensity ratio map generated from 1692 cm^{-1} (amide I) map and 1033 cm^{-1} (PO_4^{3-}-v_3) map after image shift correction with the AFM image. As indicated in Fig. 6C, the intertubular dentin exhibits relative higher amide I/ PO_4^{3-}-v_3 intensity than peritubular dentin, suggesting the amide I/ PO_4^{3-}-v_3 ratio is more abundant in intertubular dentin than in peritubular dentin, which is in accordance with the results of chemical mapping.

The Young's modulus of peritubular and intertubular dentin

Young's Modulus mapping of the longitudinal section of dentin was obtained with AFM AM-FM mode. As shown in Fig. 7A, the peritubular dentin shows a flat and smooth structure whereas the intertubular dentin has many globular structures. In the Young's modulus image (Fig. 7B), the color scale represents relative difference in the Young's modulus, differentiating between intertubular
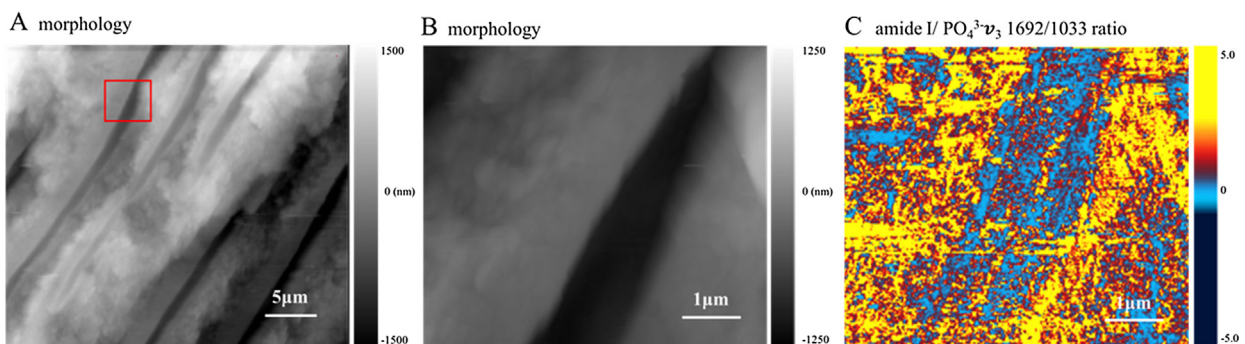
Fig. 6. The amide I/PO_4^{3-}-v_3 peak intensity ratio map of dentin generated from 1692 cm^{-1} (amide II) map and 1033 cm^{-1} (PO_4^{3-}-v_3) map after image shift correction. (A) AFM morphology (30.0×25.4 μm^2). (B) AFM morphology (5.0×4.6 μm^2). (C) The amide I/ PO_4^{3-}-v_3 peak intensity ratio map corresponds to B.
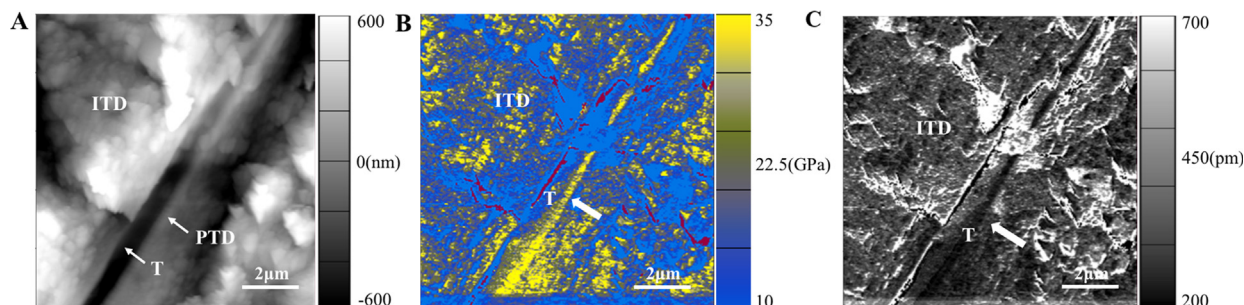
Fig. 7. Young's Modulus and indentation mapping of the longitudinal section of dentin. (A) AFM topographic image. (B) The Young's modulus image corresponds to A. (C) The indentation image corresponds to A. These three images were captured simultaneously. Areas are 10×10 μm². T, dentin tubule; ITD, intertubular dentin; PTD, peritubular dentin. White arrow in Fig. 7B and 7C indicates peritubular dentin. Scar bar: 2 μm.

dentin and peritubular dentin. In Fig. 7A, the black, roughly linear, trough-like structure going from bottom left to upper right is the dentin tubular space once occupied by the odontoblastic process. Roughly parallel to this trough-like structure is a yellow structure showing higher Young's modulus, which is the lamella of peritubular dentin observed in longitudinal section (Fig. 7B).

The peritubular dentin surrounding the dentin tubule, indicated in yellow in Fig. 7B, shows the Young's modulus value of 32.25 ± 4.67 GPa, while the intertubular dentin connecting the tubules, indicated in blue, has a Young's modulus of 20.13 ± 1.97 GPa ($p < 0.05$). Meanwhile, AM-FM imaging also provides the indentation mapping, which is shown in Fig. 7C. The average indentation values of the peritubular dentin and intertubular dentin are calculated by averaging 5 indentation values from each region, which are 0.20 ± 0.02 nm and 0.41 ± 0.09 nm, respectively ($p < 0.01$). Peritubular dentin is thus much stiffer than intertubular dentin.

The mineral/protein ratio of peritubular dentin was significantly higher compared to intertubular dentin. As for mechanical properties, peritubular dentin had a higher Young's modulus than intertubular dentin, suggesting a positive relationship exists between mineral content and mechanical properties of dentin. In accordance with our findings, it was reported that the hardness of dentin was dependent on its mineral content and reduction of dentin hardness was directly linked to the decreased mineral content [69]. Notably, as dentin heterogeneities at very small scales can be identified, mechanical information of peritubular and intertubular dentin cannot be obtained with standard physical tests. The AFM indentation method improves the accuracy of modulus at micro- and even nano-scales, due to the introduction of an experimentally determined tip area function [70].

In the present study, we employed nanoscale AFM-IR to characterize the chemical nature of human peritubular and intertubular dentin, both inorganic and organic phases, for the first time. As reported by literature, FTIR spectroscopy has been used in analyzing the organic and mineral composition in horse dentin and there was collagen in both peritubular and intertubular dentin [16]. However, Habelita et al reported that piezoresponse force microscopy (PFM) cannot detect any piezoelectric response in human peritubular dentin, thus it should be a non-collagenous tissue [8]. An invasive and destructive method of immunohistochemistry have proved that chondroitin sulfate was the typical phosphoproteins of peritubular dentin [54], which was consistent with the result of this study. Compared with previous studies, our study showed that most of organic content (amide I, II, III) and mineral content of peritubular dentin are similar to those of intertubular dentin. A distinctive band of 1336 cm^{-1} indicative of the S=O stretching vibrations (sulfonamide) was detected in peritubular dentin, but was absent in intertubular dentin. A summary of the comparison of our results with existing reports was shown in Table S1 as an attachment file [16,31,32,71,72].

As an outstanding technique in exploring the nano-topography and chemical constituents of biomaterial [23–30], AFM-IR technique can be employed for investigating the relationship of organic and inorganic components and deciphering the biochemical mineralization mechanism of dentin in the near future. Although there are excellent advantages of applying AFM-IR in directly characterizing the peritubular and intertubular dentin, we need to consider the limitation of this study. The teeth samples in this study were selected from patients between ages of 18 and 30, however, it is reported that ageing of teeth may influence the parameters of chemical components and mechanical properties [71,73]. It would be useful to analyze the heterogeneity of human dentin from different age groups in the future.

This study indicated that AFM-IR can be used in the future to analyze changes in human dentin mineral formation in health and disease (eg. dentinogenesis imperfecta). Additionally, in response to acidic and bacterial attacks, chemical characteristics such as mineral/protein ratio, crystallinity and acid phosphate content of dentin should be investigated in response to acidic and bacterial attacks.

Conclusions

We conducted AFM-IR and AM-FM analyses of human dentin which confirmed our conjecture that the chemical and mechanical properties of peritubular dentin are different from intertubular dentin. This is the first study to characterize the chemical composition and distribution of human dentin by AFM-IR technique, proving AFM-IR is a suitable and rapid method for identification of the chemical contents in human calcified tissues at nanoscale.

This study paves the way for investigating mineral deposition mechanisms of peritubular and intertubular dentin and analyzing pathological changes in dentinal structure and composition in response to acidic and bacterial attacks in future studies.

Compliance with Ethics requirements

All procedures followed were in accordance with the ethical standards of the responsible committee on human experimentation (institutional and national) and with the Helsinki Declaration of 1975, as revised in 2008 (5). Informed consent was obtained from all patients for being included in the study.

Acknowledgements

Declaration of Competing Interest

The authors deny any conflicts of interest related to this study.

Appendix A. Supplementary material

Supplementary data to this article can be found online at https://doi.org/10.1016/j.jare.2019.12.004.

References

[1] Nanci A. Chapter 8 dentin-pulp complex. In: Nanci A, 8th ed. Ten Cate's oral histology: development, structure, and function. St. Louis: Mosby Elsevier; 2008. p. 91–238.

[2] Tjäderhane L, Carrilho MR, Breschi L, Tay FR, Pashley DH. Dentin basic structure and composition: an overview. Endodontic Topics 2009;20:3–29.

[3] Weiner S, Lowenstam H. Organization of extracellularly mineralized tissues: a comparative study of biological crystal growth. Crit Rev Biochem Mol Biol 1986;20:365–408.

[4] Xu C, Wang Y. Chemical composition and structure of peritubular and intertubular human dentin revisited. Arch Oral Biol 2012;57:381–91.

[5] Kinney JH, Marshall SJ, Marshall GW. The mechanical properties of human dentin: a critical review and re-evaluation of the dental literature. Crit Rev Oral Biol 2003;14:13–29.

[6] Huang GT. Dental pulp and dentin tissue engineering and regeneration: advancement and challenge. Front Biosci (Elite Ed) 2011;3:788–800.

[7] Marshall GWJR, Marshall SJ, Kinney JH, Balooch M. The dentin substrate: structure and properties related to bonding. J Dent 1997;25:441–58.

[8] Habelitz S, Rodriguez BJ, Marshall SJ, Marshall GW, Kalinin SV, Gruverman A. Peritubular dentin lacks piezoelectricity. J Dent Res 2007;86:908–11.

[9] Salavati-Niasari M, Mohandes F, Davar F. Preparation of PbO nanocrystals via decomposition of lead oxalate. Polyhedron 2009;28:2263–7.

[10] Ren C, Qiu W, Zhang H, He Z, Chen Y. Degradation of benzene on TiO2/SiO2/Bi2O3 photocatalysts under UV and visible light. J Mol Catal A: Chem 2005;238:215–22.

[11] Zinatloo-Ajabshir S, Morassaei MS, Salavati-Niasari M. Facile fabrication of Dy2Sn2O7-SnO2 nanocomposites as an effective photocatalyst for degradation and removal of organic contaminants. J Colloid Interface Sci 2017;497:298–308.

[12] Salavati-Niasari M, Amiri A. Synthesis and characterization of alumina-supported Mn(II), Co(II), Ni(II) and Cu(II) complexes of bis(salicylaldiminato) hydrazone as catalysts for oxidation of cyclohexene with tert-buthylhydroperoxide. Appl Catal A 2005;290:46–53.

[13] Salavati-Niasari M. Zeolite-encapsulation copper(II) complexes with 14-membered hexaaza macrocycles: synthesis, characterization and catalytic activity. J Mol Catal A: Chem 2004;217:87–92.

[14] Salavati-Niasari M, Davar F. In situ one-pot template synthesis (IOPTS) and characterization of copper(II) complexes of 14-membered hexaaza macrocyclic ligand "3,10-dialkyl-dibenzo-1,3,5,8,10,12-hexaazacyclotetra-decane". Inorg Chem Commun 2006;9:175–9.

[15] Salavati-Niasari M, Davar F, Loghman-Estarki MR. Long chain polymer assisted synthesis of flower-like cadmium sulfide nanorods via hydrothermal process. J Alloy Compd 2009;481:776–80.

[16] Magne D, Guicheux J, Weiss P, Pilet P, Daculsi G. Fourier transform infrared microspectroscopic investigation of the organic and mineral constituents of peritubular dentin: a horse study. Calcif Tissue Int 2002;71:179–85.

[17] Dazzi A, Prater CB, Hu Q, Chase DB, Rabolt JF, Marcott C. AFM-IR: Combining atomic force microscopy and infrared spectroscopy for nanoscale chemical characterization. Appl Spectrosc 2012;66:1365–84.

[18] Dendisova M, Jenistova A, Parchanska-Kokaislova A, Matejka P, Prokopec V, Svecova M. The use of infrared spectroscopic techniques to characterize nanomaterials and nanostructures: a review. Anal Chim Acta 2018;15:1–14.

[19] Huth F, Schnell M, Wittborn J, Ocelic N, Hillenbrand R. Infrared-spectroscopic nanoimaging with a thermal source. Nat Mater 2011;10:352–6.

[20] Dazzi A, Prater CB. AFM-IR: Technology and applications in nanoscale infrared spectroscopy and chemical imaging. Chem Rev 2017;117:5146–73.

[21] Sauvage S, Driss A, Reveret F, Boucaud P, Dazzi A, Prazeres R, et al. Homogeneous broadening of the S to P transition in InGaAs/GaAs quantum dots measured by infrared absorption imaging with nanoscale resolution. Phys Rev B 2011;83:035302(6).

[22] Kjoller K, Felts JR, Cook D, Prater CB, King WP. High-sensitivity nanometer-scale infrared spectroscopy using a contact mode microcantilever with an internal resonator paddle. Nanotechnology 2010;21:185705.

[23] Kim SY, Khanal D, Kalionis B, Chrzanowski W. High-fidelity probing of the structure and heterogeneity of extracellular vesicles by resonance-enhanced atomic force microscopy infrared spectroscopy. Nat Protoc 2019;14:576–93.

[24] Kim SY, Khanal D, Tharkar P, Kalionis B, Chrzanowski W. None of us is the same as all of us: resolving the heterogeneity of extracellular vesicles using single-vesicle, nanoscale characterization with resonance enhanced atomic force microscope infrared spectroscopy (AFM-IR). Nanoscale Horiz 2018;3:430–8.

[25] Chouhan S, Bajpai AK, Bhatt R. Analysis of topographical parameters and interfacial interaction of zinc oxide reinforced poly (vinyl alcohol-g-

[26] James J, Unni AB, Taleb K, Chapel JP, Kalarikkal N, Varghese S, et al. Surface engineering of polystyrene–cerium oxide nanocomposite thin films for refractive index enhancement. Nano-Struct Nano-Objects 2019;17:34–42.

[27] Thomas SP, Thomas S, Bandyopadhyay S. Mechanical, atomic force microscopy and focussed ion beam studies of isotactic polystyrene/titanium dioxide composites. Compos A 2009;40:36–44.

[28] Thomas SP, Thomas S, Bandyopadhyay S. Polystyrene-Calcium Phosphate Nanocomposites: Preparation, Morphology, and Mechanical Behavior. J Phys Chem C 2009;113:97–104.

[29] Parameswaranpillai J, Thomas, S, Grohens, Y. Polymer Blends: State of the Art, New Challenges, and Opportunities. In Characterization of Polymer Blends. Wiley-VCH Verlag GmbH and Co. KGaA; 2014. p. 1–6.

[30] Parameswaran Pillai J, Pionteck J, Habler R, Sinturel C, Mathew VS, Thomas S. Effect of Cure Conditions on the Generated Morphology and Viscoelastic Properties of a Poly (acrylonitrile-butadiene-styrene) Modified Epoxy-Amine System. Ind Eng Chem Res 2012;51:2586–95.

[31] Kinney JH, Balooch M, Marshall SJ, Marshall Jr GW, Weihs TP. Hardness and Young's modulus of human peritubular and intertubular dentine. Arch Oral Biol 1996;41:9–13.

[32] Ziskind D, Hasday M, Cohen SR, Wagner HD. Young's modulus of peritubular and intertubular human dentin by nano-indentation tests. J Struct Biol 2011;174:23–30.

[33] Garcia R, Herruzo ET. The emergence of multifrequency force microscopy. Nat Nanotechnol 2012;7:217–26.

[34] Kocun M, Labuda A, Meinhold W, Revenko I, Proksch R. Fast, high resolution, and wide modulus range nanomechanical mapping with bimodal tapping mode. ACS Nano 2017;11:10097–105.

[35] Bachmann L, Diebolder R, Hibst R, Zezell DM. Infrared adsorption bands of enamel and dentin tissues from human and bovine teeth. Appl Spectrosc Rev 2003;38:1–14.

[36] Antunes A, de. Rossi W, Zezell DM. Spectroscopic alterations on enamel and dentin after nanosecond Nd:YAG laser irradiation. Spectrochim Acta A 2006;64:1142–6.

[37] Gourion-Arsiquaud S, Marcott C, Hu Q, Boskey AL. Studying variations in bone composition at nanoscale resolution: a preliminary report. Calcif Tissue Int 2014;95:413–8.

[38] Labuda A, Kocuń M, Meinhold W, Walters D, Proksch R. Generalized Hertz model for bimodal nanomechanical mapping. Beilstein J Nanotechnol 2016;7:970–82.

[39] Dresbach C, Krombholz A, Ebert M, Bagdahn J. Mechanical properties of glass frit bonded micro packages. Microsyst Technol 2006;12:473–80.

[40] Bertassoni LE, Orgel JP, Antipovao O, Swain MV. The dentin organic matrix-limitations of restorative dentistry hidden on the nanometer scale. Acta Biomater 2012;8:2419–33.

[41] Hu X, Peng Y, Sum CP, Ling J. Effects of concentrations and exposure times of sodium hypochlorite on dentin deproteination: attenuated total reflection Fourier transform infrared spectroscopy study. J Endod 2010;36:2008–11.

[42] Akgun OM, Bayari SH, Ide S, Polat GG, Kalkhoran IO. Micro- and nanoscale structures of mesiodens dentin: Combined study of FTIR and SAXS/WAXS techniques. Microsc Res Tech 2015;78:52–8.

[43] Liu Y, Wang Y. Proanthocyanidins' efficacy in stabilizing dentin collagen against enzymatic degradation: MALDI-TOF and FTIR analyses. J Dent 2013;41:535–42.

[44] Hassan I, Donati L, Stensitzki T, Keller BG, Heyne K, Imhof P. The vibrational spectrum of the hydrated alanine-leucine peptide in the amide region from IR experiments and first principles calculations. Chem Phys Lett 2018;698:227–33.

[45] Vinod KS, Periandy S, Govindarajan M. Spectroscopic [FT-IR and FT-Raman] and molecular modeling (MM) study of benzene sulfonamide molecule using quantum chemical calculations. J Mol Struct 2016;1116:226–35.

[46] Spencer P, Wang Y, Katz JL, Misra A. Physicochemical interactions at the dentin/adhesive interface using FTIR chemical imaging. J Biomed Opt 2005;10:031104.

[47] Mukherjee S, Gowen A. A review of recent trends in polymer characterization using non-destructive vibrational spectroscopic modalities and chemical imaging. Anal Chim Acta 2015;895:12–34.

[48] Belbachir K, Noreen R, Gouspillou G, Petibois C. Collagen types analysis and differentiation by FTIR spectroscopy. Anal Bioanal Chem 2009;395:829–37.

[49] Riaz T, Zeeshan R, Zarif F, IlyasvK Muhammad N, Safi SZ, et al. FTIR analysis of natural and synthetic collagen. Appl Spectrosc Rev 2018;53:703–46.

[50] de Campos Vidal B, Mello MLS. Collagen type I amide I band infrared spectroscopy. Micron 2011;42:283–9.

[51] Salavati-Niasari M, Banitaba SH. Alumina-supported Mn(II), Co(II), Ni(II) and Cu(II) bis(2-hydroxyanil)acetylacetone complexes as catalysts for the oxidation of cyclohexene with tert-butylhydroperoxide. J Mol Catal A: Chem 2003;201:43–54.

[52] Goudarzi M, Mir N, Mousavi-Kamazani M, Bagheri S, Salavati-Niasari M. Biosynthesis and characterization of silver nanoparticles prepared from two novel natural precursors by facile thermal decomposition methods. Sci Rep 2016;6:32539.

[53] Gholami T, Salavati-Niasari M, Bazarganipour M, Noori E. Synthesis and characterization of spherical silica nanoparticles by modified Stöber process assisted by organic ligand. Superlattices Microstruct 2013;61:33–41.

[54] Dorvee JR, Gerkowicz L, Bahmanyar S, Deymier-Black A, Veis A. Chondroitin sulfate is involved in the hypercalcification of the organic matrix of bovine peritubular dentin. Arch Oral Biol 2016;62:93–100.

[55] Mikami T, Kitagawa H. Biosynthesis and function of chondroitin sulfate. BBA 2013;1830:4719–33.

[56] Zinatloo-Ajabshir S, Salavati-Niasari M. Preparation of magnetically retrievable $CoFe_2O_4@SiO_2@Dy_2Ce_2O_7$ nanocomposites as novel photocatalyst for highly efficient degradation of organic contaminants. Compos B 2019;174:106930.

[57] Zinatloo-Ajabshir S, Morassaei MS, Salavati-Niasari M. Eco-friendly synthesis of $Nd_2Sn_2O_7$-based nanostructure materials using grape juice as green fuel as photocatalyst for the degradation of erythrosine. Compos B 2019;167:643–53.

[58] Zinatloo-Ajabshir S, Morassaei MS, Salavati-Niasari M. Facile synthesis of $Nd_2Sn_2O_7$-SnO_2 nanostructures by novel and environment-friendly approach for the photodegradation and removal of organic pollutants in water. J Environ Manage 2019;233:107–19.

[59] Salavati-Niasari M, Ghanbari D, Loghman-Estarki MR. Star-shaped PbS nanocrystals prepared by hydrothermal process in the presence of thioglycolic acid. Polyhedron 2012;35:149–53.

[60] Salavati-Niasari M, Ghanbari D, Davar F. Shape selective hydrothermal synthesis of tin sulfide nanoflowers based on nanosheets in the presence of thioglycolic acid. J Alloy Compd 2010;492:570–5.

[61] Zhang H, Yang J, Liang K, Li J, He L, Yang X, et al. Effective dentin restorative material based on phosphate-terminated dendrimer as artificial protein. Colloids Surf, B 2015;128:304–14.

[62] Lin CP, Lee BS, Lin FH, Kok SH, Lan WH. Phase, compositional, and morphological changes of human dentin after Nd:YAG laser treatment. J Endodontics 2001;27:389–93.

[63] Miller LM, Vairavamurthy V, Chance MR, Mendelsohn R, Paschalis EP, Betts F, et al. In situ analysis of mineral content and crystallinity in bone using infrared micro-spectroscopy of the V_4 PO_4^{3-} vibration. Biochim Biophys Acta 2001;1527:11–9.

[64] Sui T, Dluhoš J, Li T, Zeng K, Cernescu A, Landini G, et al. Structure-function correlative microscopy of peritubular and intertubular dentine. Materials (Basel) 2018;11:1493.

[65] Abou Neel EA, Aljabo A, Strange A, Ibrahim S, Coathup M, Young AM, et al. Demineralization-remineralization dynamics in teeth and bone. Int J Nanomedicine 2016;11:4743–63.

[66] Goldberg M, Kulkarni AB, Young M, Boskey A. Dentin: structure, composition and mineralization. Front Biosci (Elite Ed) 2011;3:711–35.

[67] Weiner S, Veis A, Beniash E, Arad T, W.Dillon J, Sabsay B, et al. Peritubular Dentin Formation: Crystal Organization and the Macromolecular Constituents in Human Teeth. Journal of Structural Biology 1999;126:27–41.

[68] Gotliv BA, Robach JS, Veis A. The composition and structure of bovine peritubular dentin: mapping by time of flight secondary ion mass spectroscopy. J Struct Biol 2006;156:320–33.

[69] Angker L, Nockolds C, Swain MV, Kilpatrick N. Correlating the mechanical properties to the mineral content of carious dentine–a comparative study using an ultra-micro indentation system (UMIS) and SEM-BSE signals. Arch Oral Biol 2004;49:369–78.

[70] Ferencz R, Sanchez J, Blumich B, Herrmann W. AFM nanoindentation to determine Young's modulus for different EPDM elastomers. Polym Test 2012;31:425–32.

[71] Ryou H, Romberg E, Pashley DH, Tay FR, Arola D. Importance of Age on the Dynamic Mechanical Behavior of Intertubular and Peritubular Dentin. J Mech Behav Biomed Mater 2015;42:229–42.

[72] Ryou H, Romberg E, Pashley DH, Tay FR, Arola D. Nanoscopic dynamic mechanical properties of intertubular and peritubular dentin. J Mech Behav Biomed Mater 2012;7:3–16.

[73] Arany S, Ohtani S. Age estimation by racemization method in teeth: application of aspartic acid, glutamate, and alanine. J Forensic Sci 2010;55:701–5.